Brownian motion in a nonhomogeneous force field and photonic force microscope

Giorgio Volpe,[1] Giovanni Volpe,[1] and Dmitri Petrov[1,2]

[1]*ICFO - Institut de Ciencies Fotoniques, Mediterranean Technology Park, 08860 Castelldefels (Barcelona), Spain*
[2]*ICREA - Institució Catalana de Recerca i Estudis Avançats, 08010 Barcelona, Spain*

The photonic force microscope (PFM) is an opto-mechanical technique that uses an optically trapped probe to measure forces in the range of pico to femto Newton. For a correct use of the PFM, the force field has to be homogeneous on the scale of the Brownian motion of the trapped probe. This condition implicates that the force field must be conservative, excluding the possibility of a rotational component. However, there are cases where these assumptions are not fulfilled. Here, we show how to expand the PFM technique in order to deal with these cases. We introduce the theory of this enhanced PFM and we propose a concrete analysis workflow to reconstruct the force field from the experimental time series of the probe position. Furthermore, we experimentally verify some particularly important cases, namely, the case of a conservative and of a rotational force field.

I. INTRODUCTION

A focused optical beam—an optical tweezer—allows one to manipulate a wide range of particles—including atoms, molecules, DNA fragments, living biological cells, and organelles within them—with applications to many areas, such as molecular biophysics, genetic manipulation, microassembly, and micromachines [1–3]. One of the most exciting applications has been the possibility to investigate and engineer the mechanical properties of microscopic systems—using, for example, optical traps as force transducers for mechanical measurements in biological systems [4–8].

In the early 1990s various kinds of scanning probe microscopy were already established. The scanning tunneling microscope (STM) [9] permits one, for example, to resolve at the atomic level crystallographic structures [10] and organic molecules [11]. The atomic force microscope (AFM) [12] has been successfully employed to study biological and nanofabricated structures, overcoming the diffraction limit of optical microscopes. However, all these techniques required a macroscopic mechanical device to guide the probe.

A new kind of scanning force microscope that uses an optically trapped dielectric microsphere as a probe was proposed in [13,14]. This technique was later called photonic force microscope (PFM) [15]. In a typical setup, the probe is held in an optical trap, where it performs random movements due to its thermal energy. The analysis of this thermal motion provides information about the local forces acting on the probe. The three-dimensional probe position can be recorded through different techniques, which detect its forward or backward scattered light, even though there are some issues to be taken into account in the backscattered case [16]. The most commonly used are a quadrant photodiode, a position sensing detector, or a high-speed video camera [3].

The PFM has been applied to measure forces in the range of femto to pico Newton—this is well below what can be achieved with techniques based on microfabricated mechanical cantilevers, such as AFM [17]—in many different fields with exciting applications, for example, in biophysics, thermodynamics of small systems, and colloidal physics [4–8,18–26].

For small displacements of the probe from the center of an optical trap, the restoring force is proportional to the displacement. Hence, an optical trap acts on the probe like a Hookeian spring with a fixed stiffness, which can be characterized with various methods [3,27]. The *correlation or power spectrum method*, in particular, is considered the most reliable [27], allowing one to determine the trap stiffness by applying Boltzmann statistics to the position fluctuations of the probe, relying only on the knowledge of the temperature and the viscosity of the surrounding medium [13–15,28,29].

Assuming a low Reynolds number regime [30,31], the Brownian motion of the probe in the optical trap is described by a set of Langevin equations as follows:

$$\gamma\dot{\mathbf{r}}(t) + \mathbf{K}\mathbf{r}(t) = \sqrt{2D}\gamma\mathbf{h}(t), \qquad (1)$$

where $\mathbf{r}(t)=[x(t),y(t),z(t)]$ is the probe position, $\gamma=6\pi R\eta$ is its friction coefficient, R is the probe radius, η is the medium viscosity, $\mathbf{K}$ is the stiffness matrix, $\sqrt{2D}\gamma\mathbf{h}(t) = \sqrt{2D}\gamma[h_x(t),h_y(t),h_z(t)]$ is a vector of independent white Gaussian random processes describing the Brownian forces, $D=k_BT/\gamma$ is the diffusion coefficient, T is the absolute temperature, and k_B is the Boltzmann constant. The orientation of the coordinate system can be chosen in such a way that the restoring force is independent in the three directions, i.e., $\mathbf{K}=\mathrm{diag}(k_x,k_y,k_x)$. In this reference frame the stochastic differential equations (1) are separated and without loss of generality their treatment can be restricted to the x projection of the system.

The autocorrelation function (ACF) of the solution to equations (1) in each direction reads

$$\langle x(t)x(t+\Delta t)\rangle = D\frac{\gamma}{k_x}e^{-k_x|\Delta t|/\gamma}, \qquad (2)$$

where k_x is the trap stiffness. Experimentally the trap stiffness is found by fitting the theoretical ACF (2) to the one obtained from the measurements. Using the Wiener-Khintchine theorem, the power spectral density (PSD) can now be calculated as the Fourier transform of the ACF as follows:
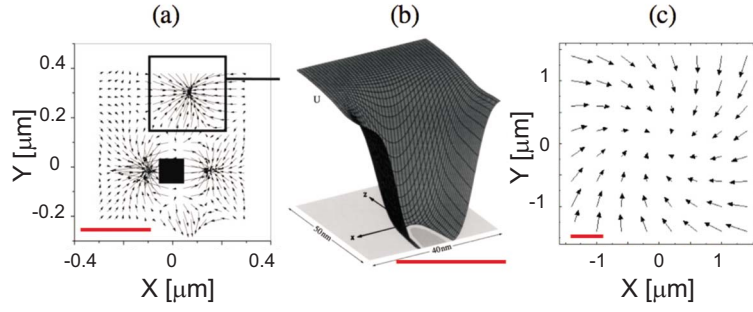
FIG. 1. (Color online) Examples of force fields that cannot be correctly probed with a classical PFM because they vary on the scale of the Brownian motion of the trapped probe, i.e., in a range of tens to hundreds of nanometers (a possible range is indicated by the red bars): (a) forces produced by a surface plasmon polariton in the presence of a patterned surface on a 50-nm-radius dielectric particle (reproduced from [32]); (b) trapping potential for a 10-nm-diam dielectric particle near a 10-nm-wide gold tip in water illuminated by a 810 nm monochromatic light beam (reproduced from [34]); and (c) force field acting on a 500-nm-radius dielectric particle in the focal plane of a highly focused Laguerre-Gaussian beam (reproduced from [35]).

$$P_x(f) = \frac{D}{2\pi^2(f^2 + f_c^2)}, \quad (3)$$

where $f_c = k_x/(2\pi\gamma)$ is the corner frequency.

A constant and homogeneous external force $f_{ext,x}$ acting on the probe produces a shift in its equilibrium position in the trap. The value of the force can be obtained as

$$f_{ext,x} = k_x \langle x(t) \rangle, \quad (4)$$

where $\langle x(t) \rangle$ is the probe mean displacement from the previous equilibrium position.

For a correct use of the PFM, the force field to measure has to be homogeneous on the scale of the Brownian motion of the trapped probe, i.e., in a range of tens to hundreds of nanometers depending on the trap stiffness. This condition implicates that the force field must be conservative, excluding the possibility of a rotational component. However, there are cases where these assumptions are not fulfilled as it is illustrated in Fig. 1. The force field can vary in the nanometer scale, for example, when one considers the force fields produced by a surface plasmon polariton [26], by a patterned optical near-field landscape at an interface decorated with resonant nanostructures [32,33] [Fig. 1(a)], or by a laser-illuminated tip [34] [Fig. 1(b)]. It can also be nonconservative in the presence of a rotational force (torque), such as the ones produced on a probe by a beam which carries orbital angular momentum [35] [Fig. 1(c)] or by certain fluid flows [36].

Here, we extend the PFM technique to deal with these cases. After introducing the theory (Sec. II), we propose a concrete analysis workflow to reconstruct the force field acting on the probe from the experimental time series of its position and we apply it to some numerically simulated data (Sec. III). Finally, we present experimental results for two fundamental cases, namely, a conservative and a rotational force field (Sec. IV).

II. THEORY

In the presence of an external force field $\mathbf{f_{ext}}(\mathbf{r}(t))$, Eq. (1) can be written in the form:

$$\gamma\dot{\mathbf{r}}(t) = \mathbf{f}(\mathbf{r}(t)) + \sqrt{2D}\gamma\mathbf{h}(t), \quad (5)$$

where the total force acting on the probe $\mathbf{f}(\mathbf{r}(t)) = \mathbf{f_{ext}}(\mathbf{r}(t)) - \mathbf{Kr}(t) = [f_x(\mathbf{r}(t)), f_y(\mathbf{r}(t))]$ depends on the position of the probe itself, but does not vary over time. We limit our analysis to a bidimensional system, because it is the most interesting from the applied point of view. However, our approach can be generalized to the tridimensional case.

The force $\mathbf{f}(\mathbf{r}(t))$ can be expanded in a Taylor series up to the first order around an arbitrary point $\tilde{\mathbf{r}}$ as follows:

$$\mathbf{f}(\mathbf{r}(t)) = \underbrace{\begin{bmatrix} f_x(\tilde{\mathbf{r}}) \\ f_y(\tilde{\mathbf{r}}) \end{bmatrix}_{\tilde{\mathbf{r}}}}_{\mathbf{f}} + \underbrace{\begin{bmatrix} \partial_x f_x(\tilde{\mathbf{r}}) & \partial_y f_x(\tilde{\mathbf{r}}) \\ \partial_x f_y(\tilde{\mathbf{r}}) & \partial_y f_y(\tilde{\mathbf{r}}) \end{bmatrix}_{\tilde{\mathbf{r}}}}_{\mathbf{J_{\tilde{r}}}}$$
$$\times [\mathbf{r}(t) - \tilde{\mathbf{r}}] + o(\|\mathbf{r} - \tilde{\mathbf{r}}\|), \quad (6)$$

where $\mathbf{f_{\tilde{r}}}$ and $\mathbf{J_{\tilde{r}}}$ are the zeroth-order expansion, i.e., the force field value at the point $\tilde{\mathbf{r}}$, and the Jacobian of the force field calculated in $\tilde{\mathbf{r}}$, respectively.

In a PFM the probe is optically trapped and, therefore, it diffuses due to Brownian motion in the total force field (the sum of the optical trapping force and external force fields). If $\mathbf{f_{\tilde{r}}} \neq \mathbf{0}$, the probe experiences a shift in the direction of the force. After a transient time has elapsed, therefore, the particle settles down in a new equilibrium position of the total force field, such that $\mathbf{f_{\tilde{r}}} = \mathbf{0}$. As seen in the Introduction, the measurement of this shift allows one to evaluate the homogeneous force acting on the probe in the standard PFM. Assuming, without loss of generality, $\tilde{\mathbf{r}} = \mathbf{0}$, the statistics of the Brownian motion near the equilibrium point can be analyzed in order to reconstruct the force field up to its first-order approximation.

We notice that, although any force field in the proximity of a potential minimum can be approximately described in the form given by Eq. (6), for the following considerations to be valid the particle motion must be confined in a potential well deep enough (at least various $k_B T$), where only one minimum is present. More complex potentials can be characterized with other techniques [37,38], which, however, cannot take into account the rotational component of the force field.
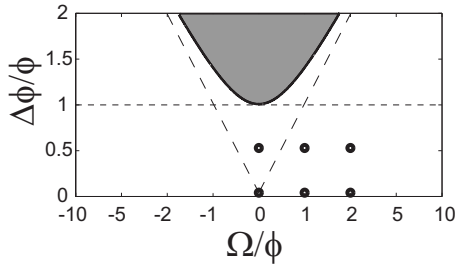
FIG. 2. Stability diagram. Assuming $\phi > 0$, the stability of the system is shown as a function of the parameters Ω/ϕ and $\Delta\phi/\phi$. The white region satisfies the stability conditions (9). The dashed lines represent the $\Delta\phi = |\Omega|$ and $\Delta\phi = \phi$ curves. The dots represent the parameters that are further investigated in Figs. 3–5.

A. Brownian motion near an equilibrium position

The first-order approximation to Eq. (5) near a stable force field equilibrium point, $\tilde{\mathbf{r}} = \mathbf{0}$, is

$$\dot{\mathbf{r}}(t) = \gamma^{-1}\mathbf{J_0}\mathbf{r}(t) + \sqrt{2D}\mathbf{h}(t), \tag{7}$$

where $\mathbf{r}(t) = [x(t), y(t)]$, $\mathbf{h}(t) = [h_x(t), h_y(t)]$, and $\mathbf{J_0}$ is the Jacobian calculated at the equilibrium point. According to the Helmholtz theorem, under reasonable regularity conditions any force field can be separated into its conservative (i.e., irrotational) and nonconservative (i.e., rotational or solenoidal) components. The two components can be identified if the coordinate system is chosen such that $\partial_y f_x(\mathbf{0}) = -\partial_x f_y(\mathbf{0})$. In this case, the Jacobian $\mathbf{J_0}$ normalized by the friction coefficient γ reads

$$\gamma^{-1}\mathbf{J_0} = \begin{bmatrix} -\phi_x & \Omega \\ -\Omega & -\phi_y \end{bmatrix}, \tag{8}$$

where $\phi_x = k_x/\gamma$ and $\phi_y = k_y/\gamma$, $k_x = -\partial_x f_x(\tilde{\mathbf{r}})$ and $k_y = -\partial_y f_y(\tilde{\mathbf{r}})$, and $\Omega = \gamma^{-1}\partial_y f_x(\tilde{\mathbf{r}}) = -\gamma^{-1}\partial_x f_y(\tilde{\mathbf{r}})$. In Eq. (8) the rotational component, which is invariant under a coordinate rotation, is represented by the nondiagonal terms of the matrix: Ω is the value of the constant angular velocity of the probe rotation around the z axis due to the presence of the rotational force field [35]. The conservative component, instead, is represented by the diagonal terms of the Jacobian and is centrally symmetric with respect to the origin. Without loss of generality, we impose that the stiffness of the trapping potential is higher along the x axis, i.e., $k_x > k_y$ and, therefore, $\phi_x > \phi_y$.

The considered equilibrium point is stable if

$$\text{Det}(\mathbf{J_0}) = \phi^2 - \Delta\phi^2 + \Omega^2 \geq 0,$$

$$\text{Tr}(\mathbf{J_0}) = -2\phi \leq 0, \tag{9}$$

where $\phi = (\phi_x + \phi_y)/2$ and $\Delta\phi = (\phi_x - \phi_y)/2$. The fundamental condition required to achieve the stability is $\phi > 0$. Assuming that this condition is satisfied, the behavior of the optically trapped probe can be explored as a function of the parameters Ω/ϕ and $\Delta\phi/\phi$. The stability diagram is shown in Fig. 2. The standard PFM corresponds to $\Delta\phi = 0$ and $\Omega = 0$. When a rotational term is added, i.e., $\Omega \neq 0$ and $\Delta\phi = 0$, the system
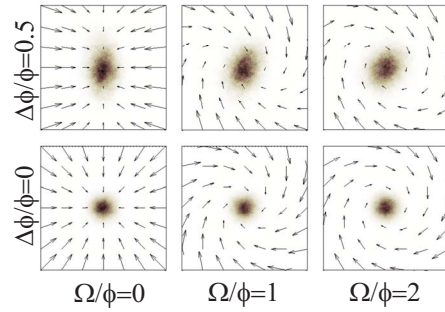

FIG. 3. (Color online) Brownian motion in a force field [Eq. (7)]. The arrows show the force field vectors for various values of the parameters $\Delta\phi/\phi$ and Ω/ϕ. The shadowed areas show the probability distribution function (PDF) of the probe position in the corresponding force field.

remains stable [35]. When there is no rotational contribution to the force field ($\Omega = 0$) the equilibrium point becomes unstable as soon as $\Delta\phi \geq \phi$. This implicates that $\phi_y < 0$, and therefore the probe is not confined in the y direction anymore. In the presence of a rotational component ($\Omega \neq 0$) the stability region becomes larger; the equilibrium point now is unstable only for $\Delta\phi \geq \sqrt{\phi^2 - \Omega^2}$.

Some examples of possible force fields are presented in Fig. 3. When $\Omega = 0$ the probe movement can be separated along two orthogonal directions. As the value of $\Delta\phi$ increases the probability density function (PDF) of the probe position becomes more and more elliptical, until for $\Delta\phi \geq \phi$ the probe is confined only along the x direction and the confinement along the y direction is lost.

If $\Delta\phi = 0$, the increase in Ω induces a bending of the force field lines and the probe movement along the x and y directions is not independent. For $\Omega \geq \phi$, the rotational component of the force field dominates over the conservative one. This is particularly clear when $\Delta\phi \neq 0$: the presence of a rotational component covers the asymmetry in the conservative one, since the PDF assumes a more rotationally symmetric shape.

B. Enhanced photonic force microscope

As we already mentioned in the Introduction, the most powerful analysis method is based on the study of the correlation functions—or, equivalently, the power spectral density—of the probe position time series. In this section, we derive the correlation matrix in the coordinate system considered in the previous section, where the conservative and rotational components are readily separated. We then derive the same matrix in a generic coordinate system and identify some functions that are independent of the choice of the coordinate system. For completeness, we will also present the power spectral density matrix.

1. Correlation matrix

The correlation matrix of the probe motion near an equilibrium position can be calculated from the solutions of Eq.

(7), whose eigenvalues are $\lambda_{1,2} = -\phi \pm \sqrt{\Delta\phi^2 - \Omega^2}$ and whose eigenvectors are $\mathbf{v_{1,2}} = [\Omega, \Delta\phi \pm \sqrt{\Delta\phi^2 - \Omega^2}]$.

Treating $\mathbf{h}(t)$ as a driving function, the solution of Eq. (7) is given by

$$\mathbf{r}(t) = \sqrt{2D} \int_{-\infty}^{t} \mathbf{W}(t)\mathbf{W}^{-1}(s)\mathbf{h}(s)\,ds, \qquad (10)$$

where

$$\mathbf{W}(t) = \begin{bmatrix} \Omega & \Omega \\ \Delta\phi + \sqrt{\Delta\phi^2 - \Omega^2} & \Delta\phi - \sqrt{\Delta\phi^2 - \Omega^2} \end{bmatrix} \begin{bmatrix} e^{\lambda_1 t} & 0 \\ 0 & e^{\lambda_2 t} \end{bmatrix} \qquad (11)$$

is the Wronskian of the system.

Since we are assuming $\mathbf{r}(t)$ to be a stationary stochastic process, the correlation matrix $\langle \mathbf{r}(t+\Delta t)\mathbf{r}^{\dagger}(t) \rangle$ can be obtained by taking the ensemble average $\langle \mathbf{r}(\Delta t)\mathbf{r}^{\dagger}(0) \rangle$ as follows:

$$\langle \mathbf{r}(\Delta t)\mathbf{r}^{\dagger}(0) \rangle = \left\langle 2D \int_{-\infty}^{\Delta t} \mathbf{W}(\Delta t)\mathbf{W}^{-1}(t')\mathbf{h}(t')\,dt' \int_{-\infty}^{0} \mathbf{h}^{\dagger}(t'')\mathbf{W}^{-1\dagger}(t'')\mathbf{W}^{\dagger}(0)\,dt'' \right\rangle, \qquad (12)$$

where the superscript $\dagger$ indicates the Hermitian. Solving this system, we have

$$r_{xx}(\Delta t) = D\frac{e^{-\phi|\Delta t|}}{\phi}\left[\left(\frac{\Omega^2 - \alpha^2\Delta\phi^2}{\Omega^2 - \Delta\phi^2} - \alpha^2\frac{\Delta\phi}{\phi}\right)\mathcal{C}(\Delta t)\right.$$
$$\left. - \alpha^2\frac{\Delta\phi}{\phi}\left(1 - \frac{\Delta\phi}{\phi}\right)\mathcal{S}(|\Delta t|)\right], \qquad (13)$$

$$r_{yy}(\Delta t) = D\frac{e^{-\phi|\Delta t|}}{\phi}\left[\left(\frac{\Omega^2 - \alpha^2\Delta\phi^2}{\Omega^2 - \Delta\phi^2} + \alpha^2\frac{\Delta\phi}{\phi}\right)\mathcal{C}(\Delta t)\right.$$
$$\left. + \alpha^2\frac{\Delta\phi}{\phi}\left(1 + \frac{\Delta\phi}{\phi}\right)\mathcal{S}(|\Delta t|)\right], \qquad (14)$$

$$r_{xy}(\Delta t) = D\frac{e^{-\phi|\Delta t|}}{\phi}\frac{\Omega}{\phi}\left[+\mathcal{S}(\Delta t) + \alpha^2\frac{\Delta\phi}{\phi}[\mathcal{C}(\Delta t) + \mathcal{S}(|\Delta t|)]\right], \qquad (15)$$

$$r_{yx}(\Delta t) = D\frac{e^{-\phi|\Delta t|}}{\phi}\frac{\Omega}{\phi}\left[-\mathcal{S}(\Delta t) + \alpha^2\frac{\Delta\phi}{\phi}[\mathcal{C}(\Delta t) + \mathcal{S}(|\Delta t|)]\right], \qquad (16)$$

where

$$\alpha^2 = \frac{\phi^2}{\phi^2 + (\Omega^2 - \Delta\phi^2)} \qquad (17)$$

is a dimensionless positive parameter,

$$\mathcal{C}(t) = \begin{cases} \cos(\sqrt{|\Omega^2 - \Delta\phi^2|}t), & \Omega^2 > \Delta\phi^2 \\ 1, & \Omega^2 = \Delta\phi^2 \\ \cosh(\sqrt{|\Omega^2 - \Delta\phi^2|}t), & \Omega^2 < \Delta\phi^2, \end{cases} \qquad (18)$$

and

$$\mathcal{S}(t) = \begin{cases} \phi\frac{\sin(\sqrt{|\Omega^2 - \Delta\phi^2|}t)}{\sqrt{|\Omega^2 - \Delta\phi^2|}}, & \Omega^2 > \Delta\phi^2 \\ \phi t, & \Omega^2 = \Delta\phi^2 \\ \phi\frac{\sinh(\sqrt{|\Omega^2 - \Delta\phi^2|}t)}{\sqrt{|\Omega^2 - \Delta\phi^2|}}, & \Omega^2 < \Delta\phi^2. \end{cases} \qquad (19)$$

In Fig. 4 these functions are plotted for different ratios of the conservative and rotational components of the force field. Some cases have already been studied experimentally. For $\Delta\phi = 0$ [35], the ACFs and cross-correlation functions (CCFs) are $r_{xx}(\Delta t) = r_{yy}(\Delta t) = De^{-\phi|\Delta t|}\cos(\Omega\Delta t)/\phi$ and $r_{xy}(\Delta t) = -r_{yx}(\Delta t) = De^{-\phi|\Delta t|}\sin(\Omega\Delta t)/\phi$, respectively. Their zeros are at $\Delta t = n\Omega/\pi$ and $\Delta t = (n+1/2)\Omega/\pi$, respectively, with n integer. However, when the rotational term is smaller than the conservative one ($\Omega < \phi$) the zeros are not distinguishable due to the rapid exponential decay of the correlation functions. As the rotational component becomes greater than the conservative one ($\Omega > \phi$), a first zero becomes visible in the ACFs and CCFs and, as Ω increases even further, the number of oscillations grows. Eventually, for $\Omega \gg \phi$ the sinusoidal component dominates. The conservative component manifests itself as an exponential decay of the magnitude of the ACFs and CCFs.

When $\Omega = 0$, the movements of the probe along the x and y directions are independent. The ACFs behave as $r_{xx}(\Delta t) = De^{-\phi_x|\Delta t|}/\phi_x$ and $r_{yy}(\Delta t) = De^{-\phi_y|\Delta t|}/\phi_y$, while the CCFs are null, $r_{xy}(\Delta t) = r_{yx}(\Delta t) = 0$. In Fig. 2 this case is represented by the line $\Omega = 0$.

When both Ω and $\Delta\phi$ are zero, the ACFs are $r_{xx}(\Delta t) = r_{yy}(\Delta t) = De^{-\phi|\Delta t|}/\phi$, and the CCFs are null, $r_{xy}(\Delta t) = r_{yx}(\Delta t) = 0$. The corresponding force field vectors point towards the center and are rotationally symmetric.

When both Ω and $\Delta\phi$ are nonvanishing, the effective angular frequency that enters the correlation functions [Eqs. (13)–(16)] is given by $\sqrt{|\Omega^2 - \Delta\phi^2|}$. Hence, the difference in the stiffness coefficients along the x and y axes effectively influences the rotational term. A limiting case is when $|\Omega| = \Delta\phi$. This case presents a kind of resonance between the rotational term and the stiffness difference.

2. Correlation matrix in a generic coordinate system

The expression for the ACFs and CCFs (13)–(16) were obtained in a specific coordinate system, where the conservative and rotational component of the force field can be readily identified. However, typically the experimentally ac-

quired time series of the probe position required for the calculation of the ACFs and CCFs are given in a different coordinate system, rotated with respect to the one considered in the previous section. If a rotated coordinate system is introduced, such that

$$\begin{bmatrix} x' \\ y' \end{bmatrix} = \begin{bmatrix} \cos\theta & -\sin\theta \\ \sin\theta & \cos\theta \end{bmatrix} \begin{bmatrix} x \\ y \end{bmatrix}, \tag{20}$$

the correlation functions in the new system are obtained as linear combinations of Eqs. (13)–(16) as follows:

$$r_{x'x'}(\Delta t) = (\cos\theta)^2 r_{xx}(\Delta t) - \cos\theta\sin\theta r_{xy}(\Delta t)$$
$$- \sin\theta\cos\theta r_{yx}(\Delta t) + (\sin\theta)^2 r_{yy}(\Delta t), \tag{21}$$

$$r_{y'y'}(\Delta t) = (\sin\theta)^2 r_{xx}(\Delta t) + \sin\theta\cos\theta r_{xy}(\Delta t)$$
$$+ \cos\theta\sin\theta r_{yx}(\Delta t) + (\cos\theta)^2 r_{yy}(\Delta t), \tag{22}$$

$$r_{x'y'}(\Delta t) = \cos\theta\sin\theta r_{xx}(\Delta t) + (\cos\theta)^2 r_{xy}(\Delta t)$$
$$- (\sin\theta)^2 r_{yx}(\Delta t) - \sin\theta\cos\theta r_{yy}(\Delta t), \tag{23}$$

$$r_{y'x'}(\Delta t) = \sin\theta\cos\theta r_{xx}(\Delta t) - (\sin\theta)^2 r_{xy}(\Delta t)$$
$$+ (\cos\theta)^2 r_{yx}(\Delta t) - \cos\theta\sin\theta r_{yy}(\Delta t), \tag{24}$$

which in general depend on θ. However, it is remarkable that the difference of the two CCFs, $D_{CCF}(\Delta t) = r_{x'y'}(\Delta t) - r_{y'x'}(\Delta t)$, and the sum of the ACFs, $S_{ACF}(\Delta t) = r_{x'x'}(\Delta t) + r_{y'y'}(\Delta t)$, are invariant as follows:

$$D_{CCF}(\Delta t) = 2D \frac{e^{-\phi|\Delta t|}}{\phi} \frac{\Omega}{\phi} \mathcal{S}(\Delta t), \tag{25}$$

$$S_{ACF}(\Delta t) = 2D \frac{e^{-\phi|\Delta t|}}{\phi} \left[\left(\frac{\Omega^2 - \alpha^2 \Delta\phi^2}{\Omega^2 - \Delta\phi^2} \right) \mathcal{C}(\Delta t) \right.$$
$$\left. + \alpha^2 \frac{\Delta\phi^2}{\phi^2} \mathcal{S}(|\Delta t|) \right]. \tag{26}$$

These functions, presented in Fig. 5, are very similar to the ones presented in Fig. 4; however, the latter depends on the coordinate system choice.

Another two combinations of Eq. (21)–(24), which are also useful for the analysis of the experimental data, namely, the sum of the CCFs, $S_{CCF}(\Delta t, \theta) = r_{x'y'}(\Delta t) + r_{y'x'}(\Delta t)$, and the difference of the ACFs, $D_{ACF}(\Delta t, \theta) = r_{x'x'}(\Delta t) - r_{y'y'}(\Delta t)$, depend on the choice of the reference frame as follows:

$$S_{CCF}(\Delta t, \theta) = 2D \frac{e^{-\phi|\Delta t|}}{\phi} \alpha^2 \frac{\Delta\phi}{\phi} [\mathcal{C}(\Delta t)$$
$$+ \mathcal{S}(|\Delta t|)] \left(\frac{\Omega}{\phi}\cos(2\theta) - \sin(2\theta) \right), \tag{27}$$

$$D_{ACF}(\Delta t, \theta) = -2D \frac{e^{-\phi|\Delta t|}}{\phi} \alpha^2 \frac{\Delta\phi}{\phi} [\mathcal{C}(\Delta t)$$
$$+ \mathcal{S}(|\Delta t|)] \left(\frac{\Omega}{\phi}\sin(2\theta) + \cos(2\theta) \right). \tag{28}$$

Their plots are shown in Fig. 6. In particular, they deliver information on the orientation θ of the coordinate system.

3. Power spectral density matrix

In the frequency domain Eq. (5) is given by

$$i2\pi f \mathbf{R}(f) = \mathbf{J_0}\mathbf{R}(f) + \sqrt{2D}\mathbf{H}(f), \tag{29}$$

and its solution is $\mathbf{R}(f) = \sqrt{2D}(i2\pi f\mathbf{I_2} - \mathbf{J_0})^{-1}\mathbf{H}(f)$, where $\mathbf{I_2}$ is the 2D unit matrix, and the corresponding PSD matrix as follows:

$$\mathbf{P}(f) = \mathbf{R}\cdot\mathbf{R}^\dagger = \frac{2D}{|(\phi_x + i2\pi f)(\phi_y + i2\pi f) + \Omega^2|^2} \begin{bmatrix} \phi_y^2 + 4\pi^2 f^2 + \Omega^2 & \Omega[\phi_x - \phi_y - i4\pi f] \\ \Omega[\phi_x - \phi_y + i4\pi f] & \phi_x^2 + 4\pi^2 f^2 + \Omega^2 \end{bmatrix}, \tag{30}$$

where the property $\mathbf{H}(f)\cdot\mathbf{H}^\dagger(f) = \mathbf{I_2}$ has been used. We notice that the PSD matrix could have been obtained as a Fourier transform of the correlation matrix (Wiener-Khintchine theorem).

III. DATA ANALYSIS WORKFLOW

In this section we propose a concrete analysis workflow to reconstruct the force field from the experimental time series of the probe position. Experimentally the time series of the probe position is the only available information to reconstruct the force field. Typically these data are obtained in an arbitrary coordinate system, generally different from the one

of Sec. II B 1. These time series need to be statistically analyzed in order to reconstruct all the parameters of the force field, i.e., ϕ, $\Delta\phi$, and Ω, and the orientation of the coordinate system. The detailed procedure to retrieve all this information from the experimental data is presented in this section.

Let us suppose one has the time series of the probe position in a generic coordinate system $\mathbf{r}'(t) = [x'(t), y'(t)]$. In the first place, we need to verify that the force field can be expressed in the form of Eq. (6) by checking that the potential well is deep enough, i.e., the particle remains in it for a long time, and the PDF has a Gaussian shape. If this is the case, we can proceed with the following analysis. First, we evaluate the parameters ϕ, $\Delta\phi$, and Ω. Then, we transform the coordinate system to the one presented in Sec. II B 1. Finally,

we reconstruct the total force field. Eventually, the trapping force field may be subtracted to retrieve the external force field under investigation.

In order to illustrate this method we proceed to analyze some numerically simulated data. The main steps of this analysis are presented in Fig. 7. In Fig. 7(a) the PDF is shown for the case of a probe in a force field with the following parameters: $\phi = 37$ s^{-1}, $\Delta\phi = 9.3$ s^{-1} (corresponding to $k_x = 43$ pN/μm and $k_y = 26$ pN/μm), $\Omega = 0$, and $\theta = 30°$. The PDF is ellipsoidal due to the difference of the stiffness along two orthogonal directions. In Fig. 7(b) the PDF for a force field with the same ϕ, $\Delta\phi$, and orientation but with $\Omega = 37$ s^{-1} is presented. The presence of the rotational component in the force field produces two main effects. First, the PDF is more rotationally symmetric and its main axes undergo a further rotation. Secondly, $D_{CCF}(\Delta t)$ is not null [Fig. 7(d)].

A. Evaluation of the parameters ϕ, $\Delta\phi$, and Ω

To evaluate the force field parameters ϕ, $\Delta\phi$, and Ω, we calculate the correlation matrix in the coordinate system where the experiment has been performed,

$$\langle \mathbf{r}'(\Delta t)\mathbf{r}'^{\dagger}(0)\rangle = \begin{pmatrix} r_{x'x'}(\Delta t) & r_{x'y'}(\Delta t) \\ r_{y'x'}(\Delta t) & r_{y'y'}(\Delta t) \end{pmatrix}. \quad (31)$$

Then we calculate $D_{CCF}(\Delta t)$. As we showed in Sec. II, this function is invariant with respect to the choice of the reference system, and it is different from zero only if $\Omega \neq 0$. The results are shown in Figs. 7(c) and 7(d) for the data shown in Figs. 7(a) and 7(b), respectively. The three aforementioned parameters can be found by fitting the experimental data to the theoretical shape of this function. In particular, the exponential decay of the function is related to the ϕ parameter; the period of the superimposed oscillations is related to the effective angular frequency $\sqrt{|\Delta\phi^2 - \Omega^2|}$; and the sign of the slope in $\Delta t = 0$ gives the sign of Ω.

When $\Omega = 0$, $D_{CCF}(\Delta t)$ is null [Fig. 7(c)]. It cannot be used to find the two remaining parameters. For $\Omega = 0$, the other invariant function is given by

$$S_{ACF}(\Delta t) = 2D\frac{e^{-\phi|\Delta t|}}{\phi}\left[\frac{\phi^2}{\phi^2 - \Delta\phi^2}\mathcal{C}(\Delta t) + \frac{\Delta\phi^2}{\phi^2 - \Delta\phi^2}\mathcal{S}(\Delta t)\right]. \quad (32)$$

ϕ and $\Delta\phi$ can be evaluated by fitting the data to Eq. (32). The function (26) can also be used for the fitting of the three parameters but cannot give information on the sign of Ω, which must be retrieved from the sign of the slope at $\Delta t = 0$ of $D_{CCF}(\Delta t)$.

B. Coordinate system transformation

Although the values of the parameters ϕ, $\Delta\phi$, and Ω are now known, the directions of the force vectors are still missing. In order to retrieve the orientation of the experimental coordinate system, we now use the orientation dependent $S_{CCF}(\Delta t, \theta)$ and $D_{ACF}(\Delta t, \theta)$. The best choice is to evaluate the two functions for $\Delta t = 0$, because the signal-to-noise ratio is highest at this point.

$$S_{CCF}(0, \theta) = 2D\frac{\alpha^2}{\phi}\frac{\Delta\phi}{\phi}\left[\frac{\Omega}{\phi}\cos(2\theta) - \sin(2\theta)\right]$$

$$D_{ACF}(0, \theta) = -2D\frac{\alpha^2}{\phi}\frac{\Delta\phi}{\phi}\left[\frac{\Omega}{\phi}\sin(2\theta) + \cos(2\theta)\right]. \quad (33)$$

The solution of this system delivers the value of the rotation angle θ. If $\Delta\phi = 0$, Eq. (33) is undetermined as a consequence of the PDF radial symmetry. In this case any orientation can be used. If $\Omega = 0$, the orientation of the coordinate system coincides with the axis of the PDF ellipsoid and, although Eq. (33) can still be used, the principal component analysis (PCA) algorithm [39] is a convenient alternative means to determine their directions.
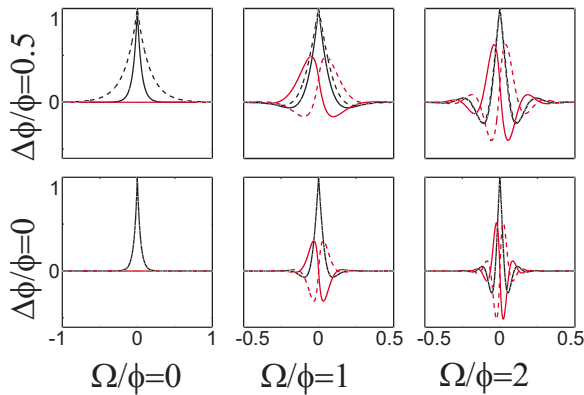

FIG. 4. (Color online) Autocorrelation and cross-correlation functions [Eqs. (13)–(16)] for various values of the parameters $\Delta\phi/\phi$ and ψ/ϕ: r_{xx} (black continuous line), r_{yy} (black dotted line), r_{xy} (gray—green in the online version–continuous line), and r_{yx} (gray—green in the online version—dotted line).
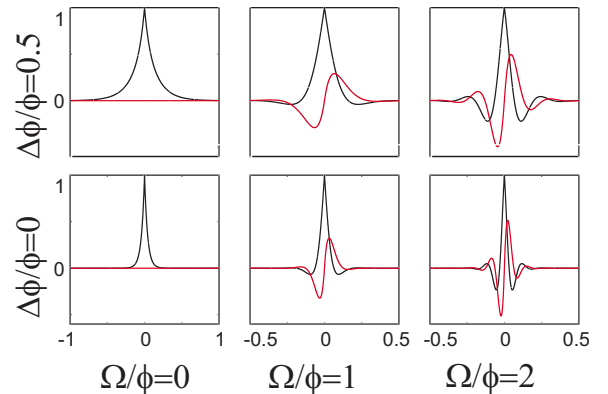

FIG. 5. (Color online) Functions (25) and (26) independent from choice of the reference system for various values of the parameters $\Delta\phi/\phi$ and Ω/ϕ: $S_{ACF}(\Delta t)$ (black line) and $D_{CCF}(\Delta t)$ (gray—green in the online version—line).
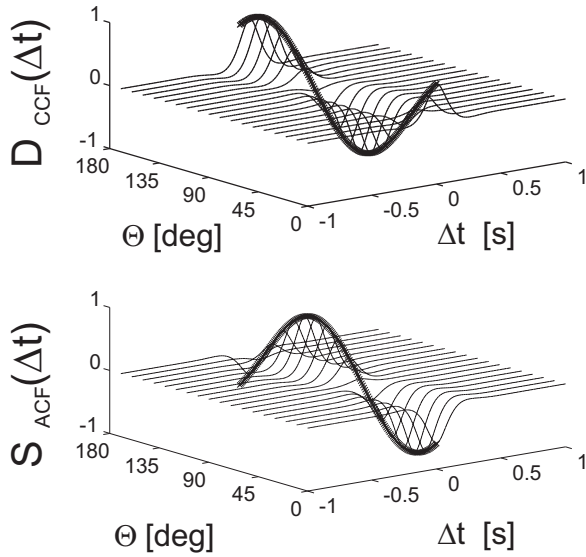
FIG. 6. Functions that depend on the orientation of the coordinate system [Eqs. (27) and (28)] for various values of the angle with respect to the coordinate system in Sec. II B 1. The markers highlight the values for $\Delta t=0$.

C. Reconstruction of the force field

Now everything is ready to reconstruct the unknown force field acting on the probe around the equilibrium position in an area comparable with the mean square displacement of the probe. From the values of ϕ and $\Delta\phi$, the conservative forces acting on the probe result $\mathbf{f}_c(x,y)=-(k_x x \mathbf{e}_x + k_y y \mathbf{e}_y)$ and, from the values of Ω, the rotational force is $\mathbf{f}_r(x,y) = \Omega(y\mathbf{e}_x - x\mathbf{e}_y)$. The total force field is

$$\mathbf{f}(x,y) = \mathbf{f}_c(x,y) + \mathbf{f}_r(x,y) = (-k_x x + \Omega y)\mathbf{e}_x - (k_y y + \Omega x)\mathbf{e}_y x. \tag{34}$$

in the rotated coordinate system [Figs. 7(e) and 7(f)]. Now the rotation (20) can be used in order to have the force field in the experimental coordinate system. The unknown component can be easily reconstructed by subtraction of the known ones, such as the optical trapping force field.

IV. EXPERIMENTAL RESULTS

For an experimental verification of our conclusions, we analyze the Brownian motion of an optically trapped polystyrene sphere in the presence of an external force field generated by a fluid flow [36]. In general a hydrodynamic flow can be decomposed into a translational (conservative) component and a vorticity (rotational) one, which are present in superposition. The data workflow described in the previous section—namely, the fitting of the parameters $\Delta\phi$ and Ω—permits one to identify and quantify the two contributions starting from the data about the Brownian motion of the probe and without any previous assumption. In this experimental section we analyze the two limiting cases, in which only one contribution is present, but we will analyze the data following the general workflow, which identifies the presence as well as the absence of each component.
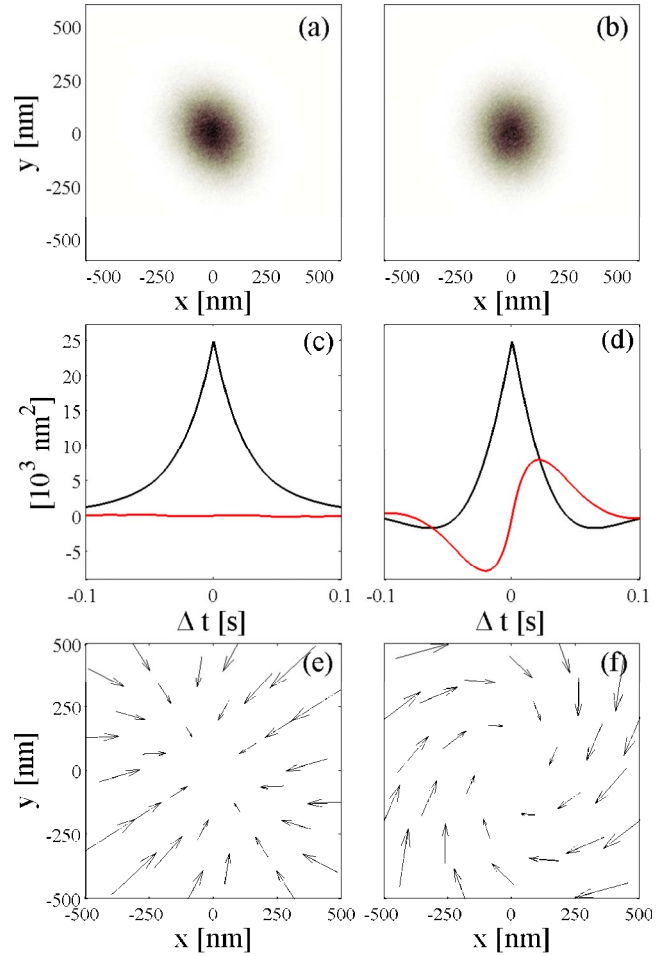

FIG. 7. (Color online) Data analysis of numerically simulated time series. [(a) and (b)] Probability density function for a Brownian particle under the influence of the force-field (simulated data 30 s at 16 kHz); in (a) the force field is purely conservative, while in (b) it has a rotational component. [(c) and (d)] Invariant function, $S_{ACF}(\Delta t)$ (black line) and $D_{CCF}(\Delta t)$ (gray—red in the online version—line) (calculated from the simulated data windowed in 1 s intervals and averaged). [(e) and (f)] Force fields reconstructed from the simulated data.

A. Experimental setup

Figure 8 illustrates a schematic of the setup.

A chamber is prepared using two cover slips separated by a 50 μm spacer, and filled with a water solution containing polystyrene spheres (radius $R=0.5$ μm) and solid spheres made of a birefringent material (calcium vaterite crystals (CVC) spheres, radius $R=1.5\pm0.2$ μm [40]).

The optical setup includes up to five independent beams: a 633 nm beam and up to four 1064 nm steerable beams with controllable polarization. The 633 nm beam generated by a HeNe laser is expanded (in order to overfill the objective) and focused by a 100×1.3 NA objective inside the chamber. This beam is used to trap a polystyrene sphere as a Brownian probe. The trap force constant can be adjusted by changing the intensity of the beam. In detecting the particle position, the forward scattered light from the trapped sphere is collimated by a $50\times$ objective onto a quadrant photodiode (QPD).
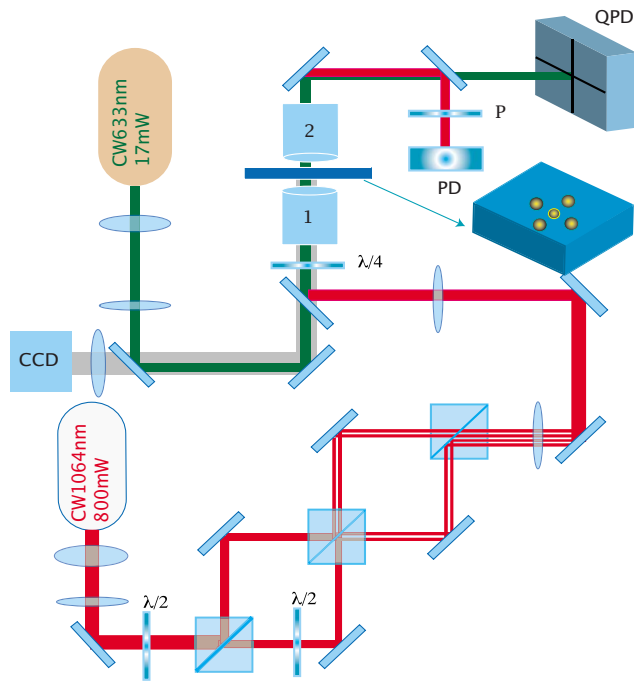
FIG. 8. (Color online) Experimental setup: 1, 100×1.3 NA objective; 2, $50\times$ objective.

The external force field acting on the probe was produced by a fluid flow generated using the spinning CVC spheres. The 1064 nm beams are generated by a Nd:YAG laser, whose maximum power is 900 mW. The beam from the laser passes through three beam splitters in a cascade obtaining four independent beams with the same power and linear polarization. A quarter wave plate is introduced along their path in order to allow one to switch the beam polarization between linear and circular. These beams are used to manipulate the CVC spheres, which can be made spin through the transfer of light orbital angular momentum [40]. They are all-optically controlled, i.e., their positions are controlled by the optical trap position, their rotation rates are controlled by the beam powers, and their spinning states are controlled by the polarization state of the light (namely, they spin in the presence of circular polarization). Their angular velocity is measured by analyzing the polarization state of the probe beam transmitted through the particle [40].

B. Conservative force field

In order to produce a conservative force field, two CVCs were placed as shown in Fig. 9(a). In Fig. 9(b) the generated hydrodynamic force field is presented as it is theoretically expected to be [36].

In Fig. 9(c), the invariant functions $S_{ACF}(\Delta t)$ (black line) and $D_{CCF}(\Delta t)$ (gray—green in the online version—line), and respective fitting to the theoretical shapes are presented. The vanishing of $D_{CCF}(\Delta t)$ tells us that $\Omega=0$ in this case, while the fitting to $S_{ACF}(\Delta)$ permits us to find the values of ϕ $=18$ s^{-1} and $\Delta\phi=6$ s^{-1}. The value of the rotation of the coordinate system in this case is $32°$.
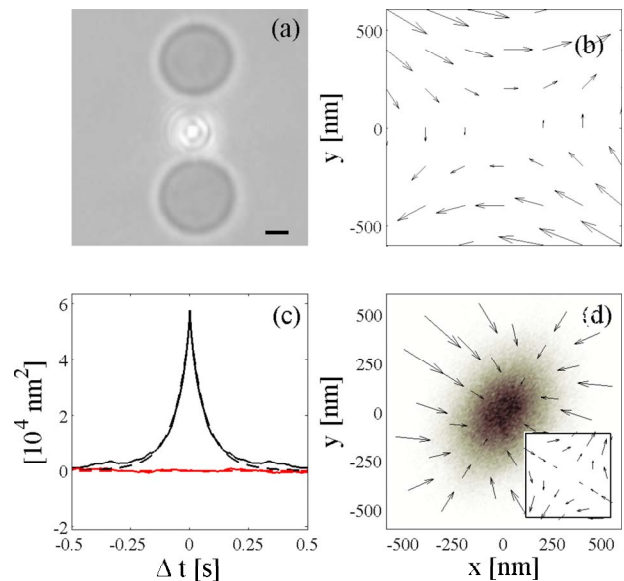

FIG. 9. (Color online) Conservative force field. (a) Experimental configuration with two spinning spheres (the horizontal x and vertical y axes are centered on the probe particle) and (b) hydrodynamic component of the force field (from hydrodynamic theory). The black bar represents a length of 1 μm. (c) Experimental invariant functions $S_{ACF}(\Delta t)$ (black line) and $D_{CCF}(\Delta t)$ (gray—red in the online version—line), and respective fitting to the theoretical shape (dotted lines). (d) Experimental probability density function and reconstructed total force field; inset: reconstructed hydrodynamic force field. The reconstruction is accurate only over the region visited by the Brownian particle. Ten datasets obtained during 15 s with sampling rate 2000 Hz were acquired and analyzed.

The total force field can now be reconstructed over the region visited by the Brownian particle: $k_x=225$ fN/μm and $k_y=112$ fN/μm. This force field is presented in Fig. 9(d). We can now retrieve the hydrodynamic force field by subtracting the optical force field ($k_{opt}=185$ fN/μm approximatively constant in all directions), which can be measured in absence of rotation of the spinning particles [inset in Fig. 9(d)]. This experimentally measured force field corresponds very well to the theoretically predicted one [Fig. 9(b)].

C. Rotational force field

In order to produce a rotational force field, four CVCs were placed as shown in Fig. 10(a), which should theoretically generate the force field shown in Fig. 10(b). In Fig. 10(c), the invariant functions $S_{ACF}(\Delta t)$ (black line) and $D_{CCF}(\Delta t)$ (gray—green in the online version—line), and respective fitting to the theoretical shapes are presented. Now $D_{CCF}(\Delta t)$ is not null and therefore it can be used to fit the three parameters: $\phi=11$ s^{-1}, $\Delta\phi\approx0$, and $\Omega=5$ rad s^{-1}. We can notice that $S_{ACF}(\Delta t)$ can be used for this purpose as well; however, in this case the sign of Ω stays undetermined.

The total force field can now be reconstructed over the region visited by the Brownian particle: $k_x\approx k_y$ $=100$ fN/μm. This force field is presented in Fig. 10(d). We can now retrieve the hydrodynamic force field by subtracting the optical force field ($k_{opt}=78$ fN/μm approximatively con-
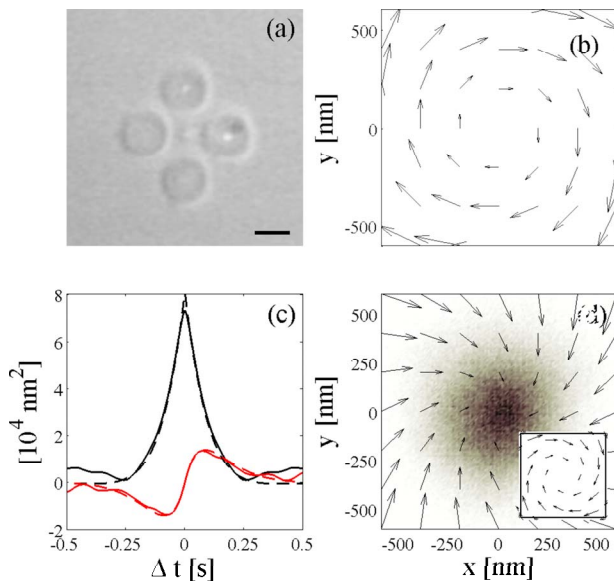
FIG. 10. (Color online) Rotational force field. (a) Experimental configuration with four spinning spheres (the horizontal x and vertical y axes are centered on the probe particle) and (b) hydrodynamic component of the force field (from hydrodynamic theory). The black bar represents a length of 3 μm. (c) Experimental invariant functions $S_{ACF}(\Delta t)$ (black line) and $D_{CCF}(\Delta t)$ (gray—red in the online version—line), and respective fitting to the theoretical shape (dotted lines). (d) Experimental probability density function and reconstructed total force field; inset: reconstructed hydrodynamic force field. The reconstruction is accurate only over the region visited by the Brownian particle. Ten datasets obtained during 15 s with sampling rate 2000 Hz were acquired and analyzed.

stant in all directions), that can be measured in absence of rotation of the spinning particles [inset in Fig. 10(d)]. Again, this experimentally measured force field corresponds very well to the theoretically predicted one [Fig. 10(b)].

V. CONCLUSION

We have shown how the PFM can be applied to the detection of locally nonhomogeneous force fields. This has been achieved by analyzing the ACFs and CCFs of the probe position time series. We believe that this technique can help to gain new insights into microscale and molecular-scale phenomena. In these cases the presence of the Brownian motion is intrinsic and cannot be disregarded. Therefore this technique permits one to take advantage of the Brownian fluctuations of the probe in order to explore the force field present in its surroundings.

One of the most remarkable advantages of the technique we propose is that it can be implemented in all existing PFM setups and even on data acquired in the past. Indeed, it does not require changes to be made in the physical setup, but only to analyze the data in a new way. This method can indeed even be applied to the study of the Brownian particle trajectories that can be obtained with techniques different from the PFM technique. The main requisite is that the particle is confined around a stable equilibrium position where the first-order Taylor expansion of the force field (6) is a good approximation.

[1] A. Ashkin, Phys. Rev. Lett. **24**, 156 (1970).

[2] A. Ashkin, J. M. Dziedzic, J. E. Bjorkholm, and S. Chu, Opt. Lett. **11**, 288 (1986).

[3] K. C. Neuman and S. M. Block, Rev. Sci. Instrum. **75**, 2787 (2004).

[4] A. Ashkin, K. Shutze, J. M. Dziedzic, U. Euteneuer, and M. Schliwa, Nature (London) **348**, 346 (1990).

[5] S. M. Block, L. S. B. Goldstein, and B. J. Schnapp, Nature (London) **348**, 348 (1990).

[6] K. Svoboda, C. F. Schmidt, B. J. Schnapp, and S. M. Block, Nature (London) **365**, 365 (1993).

[7] S. C. Kuo and M. P. Sheetz, Science **260**, 232 (1993).

[8] J. T. Finer, R. M. Simmons, and J. A. Spudich, Nature (London) **368**, 113 (1994).

[9] G. Binnig, H. Rohrer, C. Gerber, and E. Weibel, Phys. Rev. Lett. **49**, 57 (1982).

[10] G. Binnig, H. Rohrer, C. Gerber, and E. Weibel, Phys. Rev. Lett. **50**, 120 (1983).

[11] D. P. E. Smith, J. K. H. Höber, G. Binnig, and H. Nejoh, Nature (London) **344**, 641 (1990).

[12] G. Binnig, C. F. Quate, and C. Gerber, Phys. Rev. Lett. **56**, 930 (1986).

[13] L. P. Ghislain and W. W. Webb, Opt. Lett. **18**, 1678 (1993).

[14] L. P. Ghislain, N. A. Switz, and W. W. Webb, Rev. Sci. Instrum. **69**, 2762 (1994).

[15] E.-L. Florin, A. Pralle, J. K. H. Hörber, and E. H. K. Stelzer, J. Struct. Biol. **119**, 202 (1997).

[16] G. Volpe, G. Kozyreff, and D. Petrov, J. Appl. Phys. **102**, 084701 (2007).

[17] A. L. Weisenhorn, P. K. Hansma, T. R. Albrecht, and C. F. Quate, Appl. Phys. Lett. **54**, 2651 (1989).

[18] A. Prälle, E.-L. Florin, E. H. K. Stelzer, and J. K. H. Höber, Appl. Phys. A: Mater. Sci. Process. **66**, S71 (1998).

[19] A. D. Menta, M. Rief, J. A. Spudich, D. A. Smith, and R. M. Simmons, Science **283**, 1689 (1999).

[20] A. Prälle, E.-L. Florin, E. H. K. Stelzer, and J. K. H. Hörber, Single Mol. **1**, 129 (2000).

[21] D. E. Smith, S. J. Taus, S. B. Smith, S. Grimes, D. L. Ander-

son, and C. Bustamante, Nature (London) **413**, 748 (2001).

[22] M. J. Lang, C. L. Asbury, J. W. Shaevitz, and S. M. Block, Biophys. J. **83**, 491 (2002).

[23] S. B. Smith, Y. Cui, and C. Bustamante, Methods Enzymol. **361**, 134 (2003).

[24] A. Rohrbach, Opt. Express **13**, 9695 (2005).

[25] G. Volpe, G. P. Singh, and D. Petrov, Appl. Phys. Lett. **88**, 231106 (2006).

[26] G. Volpe, R. Quidant, G. Badenes, and D. Petrov, Phys. Rev. Lett. **96**, 238101 (2006).

[27] K. Visscher, S. P. Gross, and S. M. Block, IEEE J. Sel. Top. Quantum Electron. **2**, 1066 (1996).

[28] A. Rohrbach and E. H. K. Stelzer, J. Appl. Phys. **91**, 5474 (2002).

[29] K. Berg-Sørensen and H. Flyvbjerg, Rev. Sci. Instrum. **75**, 594 (2004).

[30] E. M. Purcell, Am. J. Phys. **45**, 3 (1977).

[31] J. Happel and H. Brenner, *Low Reynolds Number Hydrody-namics* (Springer, New York, 1983).

[32] R. Quidant, D. Petrov, and G. Badenes, Opt. Lett. **30**, 1009 (2005).

[33] M. Righini, A. S. Zelenina, C. Girard, and R. Quidant, Nat. Phys. **3**, 477 (2007).

[34] L. Novotny, R. X. Bian, and X. S. Xie, Phys. Rev. Lett. **79**, 645 (1997).

[35] G. Volpe and D. Petrov, Phys. Rev. Lett. **97**, 210603 (2006).

[36] G. Volpe, G. Volpe, and D. Petrov, e-print arXiv:0707.3546.

[37] H. M. K. Sasaki and M. Tsukima, Appl. Phys. Lett. **71**, 37 (1997).

[38] V. Blickle, T. Speck, U. Seifert, and C. Bechinger, Phys. Rev. E **75**, 060101(R) (2007).

[39] R. O. Duda, P. E. Hart, and D. G. Stork, *Pattern Classification* (Wiley International, New York, 2002).

[40] A. I. Bishop, T. A. Nieminen, N. R. Heckenberg, and H. Rubinsztein-Dunlop, Phys. Rev. Lett. **92**, 198104 (2004).